Bioactive Materials 8 (2022) 409–419

Contents lists available at ScienceDirect

Bioactive Materials

journal homepage: www.sciencedirect.com/journal/bioactive-materials

Titanium carbide nanosheets with defect structure for photothermal-enhanced sonodynamic therapy

Guangqiang Li [a,b], Xiaoyan Zhong [c], Xianwen Wang [b], Fei Gong [b], Huali Lei [b], Yangkai Zhou [b], Chengfei Li [a], Zhidong Xiao [a,**], Guoxi Ren [d], Liang Zhang [b], Zhiqiang Dong [e,***], Zhuang Liu [b], Liang Cheng [b,*]

[a] College of Science, State Key Laboratory of Agricultural Microbiology, Huazhong Agricultural University, Wuhan, 430070, China
[b] Institute of Functional Nano & Soft Materials (FUNSOM), Jiangsu Key Laboratory for Carbon-Based Functional Materials & Devices, Soochow University, Suzhou, 215123, China
[c] Department of Toxicology, School of Public Health, Medical College of Soochow University, Suzhou, 215123, China
[d] State Key Laboratory of Functional Materials for Informatics, Shanghai Institute of Microsystem and Information Technology, Chinese Academy of Sciences, Shanghai, 200050, China
[e] College of Biomedicine and Health, College of Life Science and Technology, Huazhong Agricultural University, Wuhan, Hubei, 430070, China

ARTICLE INFO

Keywords:
Ti_3C_2 MXenes
Oxygen defect
Sonosensitizers
Sonodynamic therapy
Biosafety

ABSTRACT

Sonodynamic therapy (SDT) has attracted widespread interest in biomedicine, owing to its novel and noninvasive therapeutic method triggered by ultrasound (US). Herein, the Ti_3C_2 MXene nanosheets (Ti_3C_2 NSs) are developed as good sonosensitizers via a two-step method of chemical exfoliation and high-temperature treatment. With the high-temperature treatment, the oxygen defect of Ti_3C_2 MXene nanosheets (H–Ti_3C_2 NSs) is greatly increased. Therefore, the electron (e^-) and hole (h^+) generated by US can be separated faster due to the improved degree of oxidation, and then the recombination of e^--h^+ can be prevented with the abundant oxygen defect under US irradiation, which induced the sonodynamic efficiency greatly to improve around 3.7-fold compared with Ti_3C_2 NSs without high-temperature treatment. After PEGylation, the H–Ti_3C_2-PEG NSs show good stability and biocompatibility. *In vitro* studies exhibit that the inherent property of mild photothermal effect can promote the endocytosis of H–Ti_3C_2-PEG NSs, which can improve the SDT efficacy. *In vivo* studies further display that the increased blood supply by the mild photothermal effect can significantly relieve hypoxia in the tumor microenvironment, showing photothermal therapy (PTT) enhanced SDT. Most importantly, the H–Ti_3C_2-PEG NSs can be biodegraded and excreted out of the body, showing no significant long-term toxicity. Our work develops the defective H–Ti_3C_2 NSs as high-efficiency and safe sonosensitizers for photothermal-enhanced SDT of cancer, extending the biomedical application of MXene-based nanoplatforms.

1. Introduction

Sonodynamic therapy (SDT), which can generate reactive oxygen species (ROS) by sonosensitizers under ultrasound (US) irradiation, has been rapidly developed and recognized as a novel and noninvasive therapeutic method for cancer treatment [1–4]. Compared with other cancer therapy methods, the US with highly focused property, high tissue penetration depth, and minimal damage to the normal tissues, has widely been used for diagnostic and treatment in clinics [5–10]. Therefore, compared with light excited photodynamic therapy (PDT) that is usually applied in superficial tumors, the US affords SDT with the preponderances in the therapy of deep-seated tumors [11–13]. As a major component in SDT, currently, the sonosensitizers are consisted of organic sonosensitizers and inorganic ones, and the efficiency of sonosensitizers plays an important role in ROS generation [1,14]. The organic sonosensitizers are mainly come from organic photosensitizers,

Peer review under responsibility of KeAi Communications Co., Ltd.
* Corresponding author.
** Corresponding author.
*** Corresponding author.
E-mail addresses: zdxiao@mail.hzau.edu.cn (Z. Xiao), dongz@mail.hzau.edu.cn (Z. Dong), lcheng2@suda.edu.cn (L. Cheng).

https://doi.org/10.1016/j.bioactmat.2021.06.021
Received 9 May 2021; Received in revised form 14 June 2021; Accepted 20 June 2021
Available online 30 June 2021

such as porphyrins [14,15] (hematoporphyrin, phtotofrin, etc.), Rose Bengal [16], and so on, while the inorganic sonosensitizers mainly include Ti-based nanomaterials [17–19], bimetallic oxide nanoparticles [20], black phosphorus [21], and so on. However, the organic sonosensitizers suffer from the fast obliteration and poor tumor accumulation, which severely restrict the efficacy of SDT [1]. Although these shortcomings can be overcome by the drug delivery system, the intrinsic issues such as photobleaching and phototoxicity still exist in organic sonosensitizer-based SDT. Fortunately, the inorganic sonosensitizers show advantages in high acoustic stability and good sonodynamic effect, however, the biosafety must be considered, and the conversion efficiency of ROS can't be ignored especially [11,22]. Therefore, more efforts of developing inorganic sonosensitizers with high efficiency and good safety should be made at this stage.

From another perspective, tumor microenvironment (TME), with the special characteristics of hypoxia, ischemia, weak acidity, and high

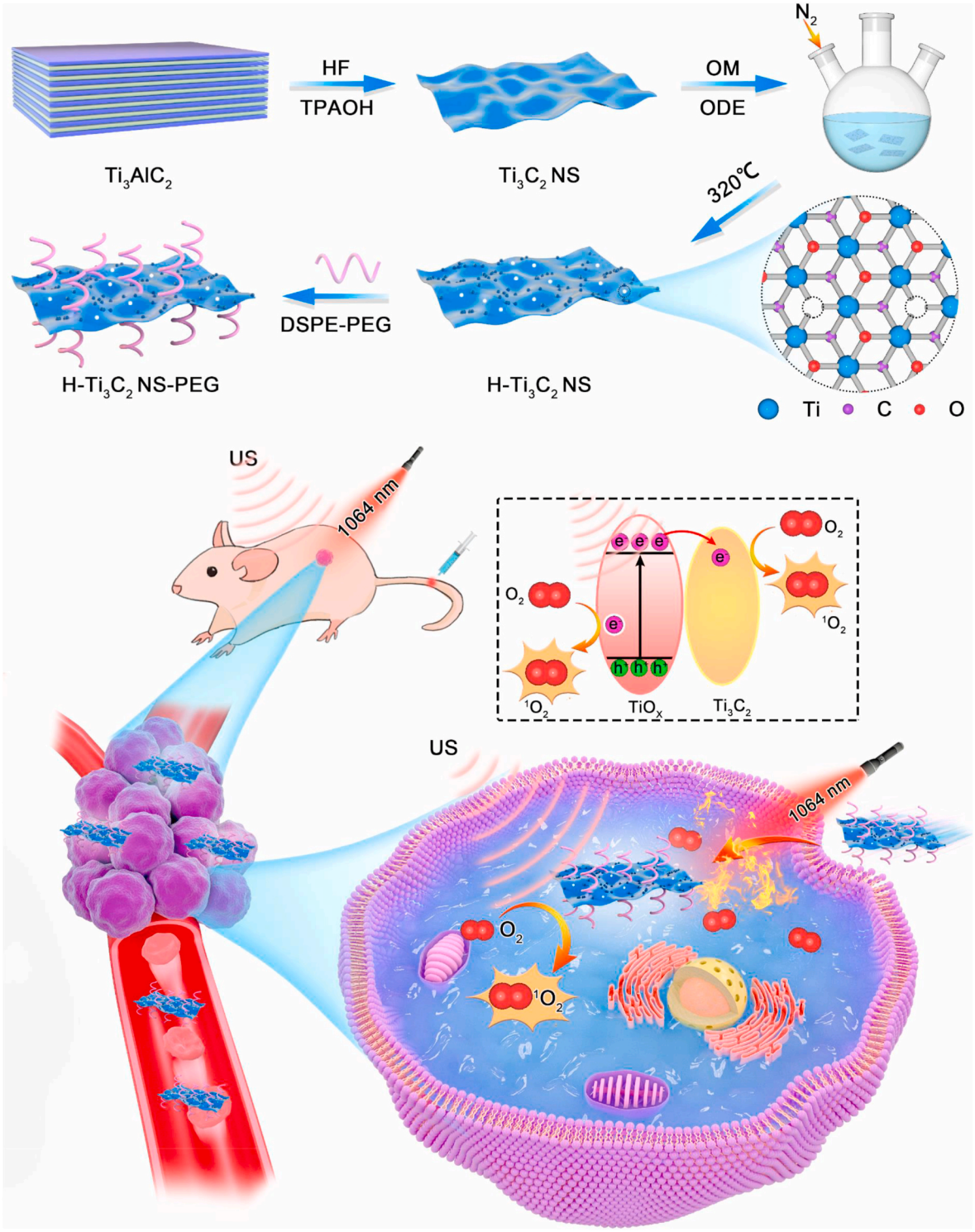

Scheme 1. Schematic of the preparation of H_H-Ti_3C_2 nanosheets by the chemical exfoliation and high-temperature treatment methods for photothermal enhanced sonodynamic cancer therapy.

concentration of hydrogen peroxide (H_2O_2) [23,24], is the natural barrier for cancer treatment, especially for oxygen (O_2)-dependent cancer treatments such as PDT [25], chemodynamic therapy (CDT) [5,26], radiotherapy (RT) [27–29], and SDT [1,30–32]. For example, the ROS yield would be significantly restricted by severe hypoxia and ischemia, and the condition of tumor hypoxia would be further accentuated with the O_2 consumption during SDT, which causes the vicious cycle and unsatisfied outcome. Therefore, it's meaningful to modulate TME, such as relieving hypoxia and ischemia, to improve the efficacy of SDT. Up to now, several strategies have appeared for tumor-hypoxia relief, like converting high content of H_2O_2 to O_2 in the TME [33], transporting O_2 to the tumor site through the fluorocarbons-based delivery system [34], increasing the blood supply to the tumor site by the mild photothermal effect [22], and so on. Owing to the limited endogenous H_2O_2 in tumor and weak transportation efficiency of O_2 to the tumor sites, the photothermal effect to ameliorate the tumor-hypoxia microenvironment is the simplest and convenient way.

Transition metal carbides, nitrides, and carbonitrides (MXenes) are a novel type of two-dimensional (2D) nanomaterials owing to their large surface area, high near-infrared (NIR) absorbance, and substitutable components ability, which have been rapidly used in biomedicine [35]. Amongst MXenes, titanium carbides (Ti_3C_2) is one of the most popular representatives with high absorbance in the NIR II region, which has been widely applied in photo-induced cancer therapy [36–38]. Due to easier to be partly oxidized of the surface on Ti_3C_2 NSs, the formation of defect structure, that was TiO_2/Ti_3C_2, could promote the transformation of charge carriers and capture the electron (e^-) to prevent the recombination of the e^- and hole (h^+), which resulted in the improved photocatalysis owing to the favorable properties [39–41]. Therefore, such unique structure would be better for US-induced cancer therapy. Herein, we developed a new type of MXene-based sonosensitizer by two-step methods of chemical exfoliation and high-temperature treatment for enhanced SDT (Scheme 1). After the high-temperature treatment of Ti_3C_2 NSs (H–Ti_3C_2 NSs), the formed TiO_x/Ti_3C_2 structure could not only promote the separation of US generated e^- and h^+ from the energy-band structure, but also capture electronic to prevent the recombination of e^--h^+ by oxygen vacancy, leading to an excellent sonodynamic effect under US irradiation. Especially, the H–Ti_3C_2 NSs also had relatively high absorbance in NIR II window, which could be used for photothermal therapy (PTT). The mild photothermal effect generated by H–Ti_3C_2 NSs could prolong the blood circulation and improve the O_2 supply. Both *in vitro* and *in vivo* photothermal-sonodynamic synergistic therapy was achieved by H–Ti_3C_2 NSs with sequential 1064 nm laser and US irradiation. Importantly, the synthesized H–Ti_3C_2-PEG NSs showed excellent biocompatibility, without causing any long-term toxicity obviously. Collectively,

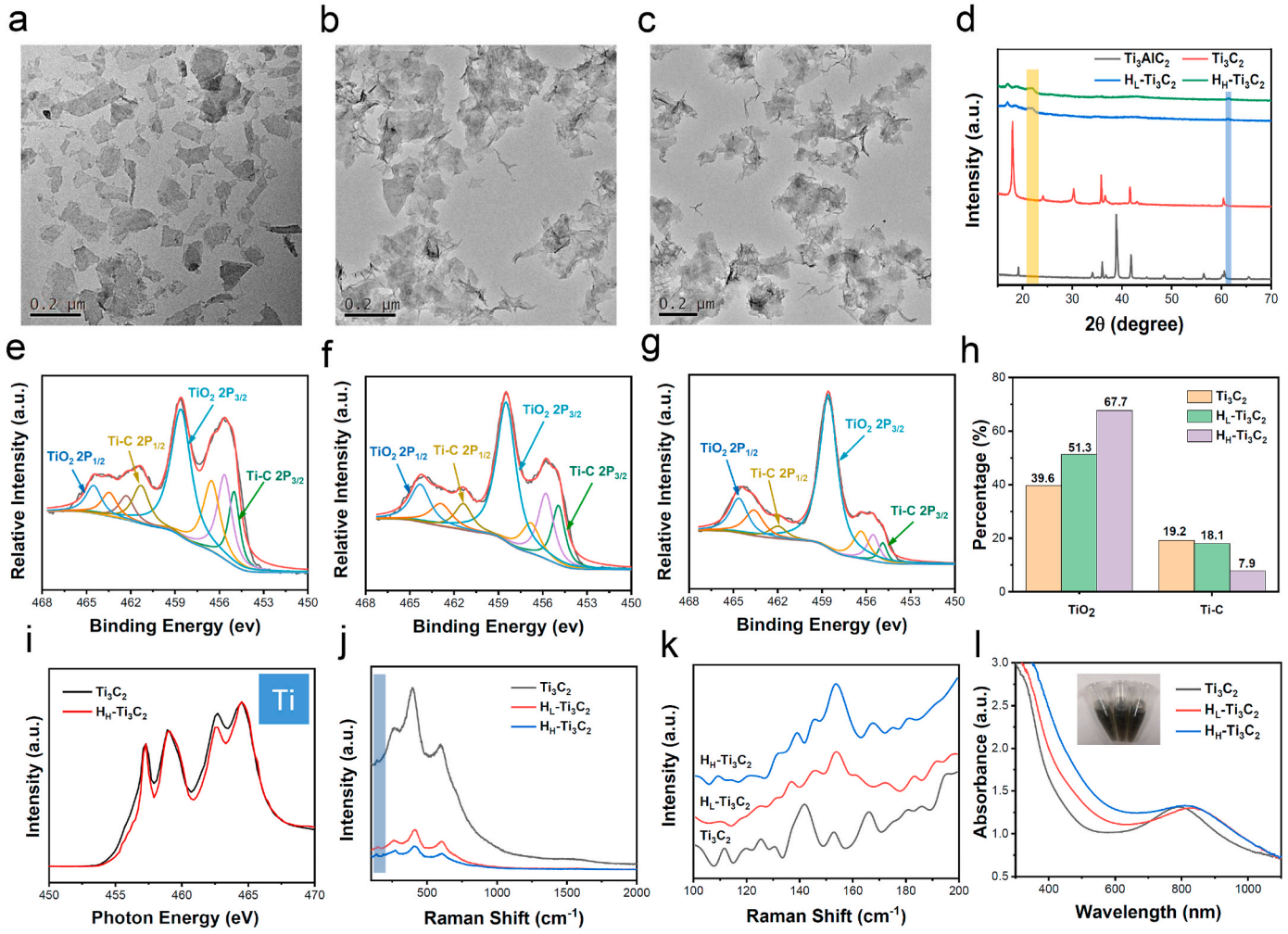

Fig. 1. Preparation and characterization of Ti_3C_2 NSs and H–Ti_3C_2 NSs prepared by high-temperature method. (**a-c**) The TEM images of Ti_3C_2 NSs (**a**), H_L-Ti_3C_2 NSs (**b**), and H_H-Ti_3C_2 NSs (**c**). (**d**) XRD spectra of Ti_3AlC_2, Ti_3C_2 NSs, H_L-Ti_3C_2 NSs, and H_H-Ti_3C_2 NSs. (**e-h**) XPS spectra of Ti 2p for Ti_3C_2 NSs (**e**), H_L-Ti_3C_2 NSs (**f**), and H_H-Ti_3C_2 NSs (**g**) and corresponding peaks area (**h**). (**i**) The NEXAFS spectra of Ti L-edge for Ti_3C_2 NSs and H_H-Ti_3C_2 NSs. (**j&k**) The Raman spectra of Ti_3C_2 NSs, H_L-Ti_3C_2 NSs, and H_H-Ti_3C_2 NSs (**j**) and corresponding magnification in the blue area (**k**). (**l**) UV–vis–NIR spectra of Ti_3C_2 NSs, H_L-Ti_3C_2 NSs, and H_H-Ti_3C_2 NSs. Insert is the photograph of Ti_3C_2 NSs, H_L-Ti_3C_2 NSs, and H_H-Ti_3C_2 NSs at the same concentration of Ti ions.

our work highlighted that the defective H–Ti_3C_2 NSs via the high-temperature treatment could be a promising sonosensitizer for SDT, which extended the biological application of MXene-based nanoplatforms.

2. Results and discussion

2.1. Preparation and characterization of Ti_3C_2 NSs and H–Ti_3C_2 NSs

According to the previous reports, Ti_3C_2 NSs were fabricated by selective etching and chemical exfoliation methods [37,38], and their morphology was mainly single-layer sheet structure revealed by transmission electron microscopy (TEM) image (Fig. 1a). Inspired by the photocatalysis application, the high-temperature method was introduced to treat the above-synthesized Ti_3C_2 NSs. In short, the Ti_3C_2 NSs were dispersed in the mixture of oleylamine (OM) and 1-octadecene (ODE), and then the solution was heated to 320 °C under nitrogen protection. In order to investigate the oxidation degree, the Ti_3C_2 NSs were treated with 1 h (H_L-Ti_3C_2 NSs) and 2 h (H_H–Ti_3C_2 NSs) at such high temperature, respectively. From the TEM images, the microstructure and morphology of Ti_3C_2 NSs did not change too much after high-temperature treatment (Fig. 1b and c). Next, the composition of Ti_3C_2 NSs before and after high-temperature treatment were carefully investigated. X-ray energy dispersive spectrometer (EDS) and element mapping firstly showed that both Ti_3C_2 NSs and H–Ti_3C_2 NSs mainly contained three elements of Ti, C, and O (Fig. S1, S2). Before the high-temperature treatment, the element O existed in the Ti_3C_2 NSs probably due to a certain degree of oxidization in the process of fabricating Ti_3C_2 NSs. With the increased time of high-temperature treatment, the content of O was gradually enhanced, demonstrating the oxidation of Ti_3C_2 NSs. From the X-ray powder diffraction (XRD) spectra, new peaks at 21.7° (TiO_2, JCPDS. 00-049-1433) and 61.1° (TiO, JCPDS. 01-086-2352) appeared (Fig. 1d), further claimed the oxidization of Ti_3C_2 NSs in the process of high-temperature treatment.

In addition, the major elements of Ti, C, and O of Ti_3C_2 NSs before and after high-temperature treatment were analyzed by X-ray photoelectron spectroscopy (XPS). For the Ti 2p region, the peaks at 455, 455.64, 456.52, 458.59, 461.3, 462.29, 463.45, and 464.51 eV corresponded to the Ti–C ($2p_{3/2}$), Ti^{2+} ($2p_{3/2}$), Ti^{3+} ($2p_{3/2}$), TiO_2 ($2p_{3/2}$), Ti–C ($2p_{1/2}$), Ti^{2+} ($2p_{1/2}$), Ti^{3+} ($2p_{1/2}$), and TiO_2 ($2p_{1/2}$), respectively (Fig. 1e–g, Fig. S3). From the spectra, we found that the peak of Ti–O band gradually increased while the Ti–C bond decreased with the high-temperature treatment. By calculating the integral area, the peak area of Ti–O band increased from ~39.6% to ~51.3% (H_L-Ti_3C_2 NSs), and further to ~67.7% (H_H–Ti_3C_2 NSs), while those of the Ti–C bond decreased from ~19.2% to ~18.1%, then to ~7.9%, respectively, indicating that the Ti_3C_2 NSs were oxidized to form TiO_x by the high-temperature treatment (Fig. 1h). In addition, the C 1s region possessed two main peaks at 281.34 and 284.92 eV, which corresponded to the Ti–C and C–C bonds, respectively (Fig. S4). The intensity of Ti–C bond also decreased gradually with the prolonged time of high-temperature treatment, indicating that the Ti_3C_2 NSs were partly transformed into TiO_x. Besides, the changes of O1s spectra revealed that the peak intensity of TiO_x increased after high-temperature treatment compared with Ti_3C_2 NSs without treatment, further indicating that the formation of TiO_x on the surface of Ti_3C_2 NSs (Fig. S5). In order to further prove the change of composition, the Ti L-edge near-edge X-ray absorption fine structure (NEXAFS) was used to identify the Ti 3d electronic state changes on the surface of Ti_3C_2 NSs before and after high-temperature treatment. There were slight changes within 455–457 eV (Fig. 1i, Fig. S6), which was caused by the crystal-field splitting of the Ti 3d oribitals, and the formed TiO_x nanostructures were sensitive to the oxidation state [42].

Raman spectrum was a significant method to analyze the surface message and the change process of nanomaterials. According to the Raman spectra, there were three characteristic peaks around 260, 400, and 600 cm^{-1} for Ti_3C_2 NSs; meanwhile, a new peak around 155 cm^{-1} appeared in the samples after the high- temperature treatment, and the intensity increased with the long-time treatment (Fig. 1j and k), which demonstrated that the TiO_x was generated and accumulated on the surface of Ti_3C_2 NSs [39,40,43]. From the UV–vis–NIR absorbance spectra, all the samples before/after high-temperature treatment showed good NIR II absorbance, which could be used for NIR II photo-induced cancer therapy. By the high-temperature treatment, the absorbance spectra and the color of samples slightly changed (Fig. 1l), indicating such treatment did not affect the unique photo properties of Ti_3C_2 NSs. Collectively, it could be directly or indirectly identified that the TiO_x were generated and accumulatively deposited on the surface of Ti_3C_2 NSs by the high-temperature treatment.

In order to improve the dispersity, stability, and promote biomedical applications, the amphiphilic polymer of DSPE-PEG $_{(2000)}$ was used to modify H–Ti_3C_2 NSs (H–Ti_3C_2-PEG NSs) by noncovalent interaction. After the surface coating, the dynamic light scattering (DLS) of the H–Ti_3C_2-PEGNSs showed an average size of ~164 nm (Fig. S7), and the final sample showed high stability in the different physiological solutions including H_2O, PBS, 0.9% NaCl, and RPMI in 4 °C (Fig. S8). Through this high-temperature treatment in the organic phase, the PEGylated H–Ti_3C_2 NSs showed excellent stability and biocompatibility, which would be used in the field of biomedicine.

2.2. Sonodynamic and photothermal performance of H–Ti_3C_2-PEG NSs

After high-temperature treatment for Ti_3C_2 NSs, the TiO_x was generated on the surface of Ti_3C_2 NSs due to the changes of composition and structure, making the H–Ti_3C_2-PEG NSs to be promising effective sonosensitizers (Fig. 2a). To investigate the sonodynamic efficiency of H–Ti_3C_2-PEG NSs, the 1,3-diphenylisobenzofuran (DPBF) was used as the molecular probe to detect ROS under US irradiation. In the presence of ROS, the characteristic peak at 418 nm decreased. The Ti_3C_2 NSs, H_L-Ti_3C_2-PEG NSs, and H_H-Ti_3C_2-PEG NSs were irradiated by US at the same condition, respectively. Compared with Ti_3C_2 NSs and commercial TiO_2, both H_L-Ti_3C_2-PEG NSs and H_H-Ti_3C_2-PEG NSs could obviously decrease the absorbance of DPBF (Fig. 2b c, Fig. S9), and the attenuation ratios were calculated to be ~18% for H_2O, ~23% for Ti_3C_2 NSs, ~45% for the commercial TiO_2, ~64% for H_L-Ti_3C_2-PEG NSs, and ~85% for H_H-Ti_3C_2-PEG NSs) after US irradiation for 6 min (Fig. 2d), indicating that the H–Ti_3C_2-PEG NSs had much stronger efficiency of ROS generation than that of Ti_3C_2 NSs and the commercial TiO_2. The longer time of high-temperature treatment, the higher the sonodynamic effect of the H–Ti_3C_2-PEG NSs. The H_H-Ti_3C_2-PEG NSs incubated with DPBF without US irradiation showed no ROS generation (Fig. S10). In addition, we also used the probe of diphenylamine (DPA) to verify the ROS ($^1O_2$) generation, it was clear that the H_H-Ti_3C_2-PEG NSs under US could generate enough $^1O_2$ (Fig. S11). Afterwards, the tetramethylbenzidine (TMB) and o-phenylenediamine (OPD) probes were also used to detect other types of ROS, like hydroxyl radical (·OH), however, no obvious signal could be detected (Fig. S12), indicated no ·OH generation under US irradiation. Moreover, electron spin resonance (ESR) measurements were further conducted to further identify the ROS type generated in this process. Obviously, the typical characteristic peak of 1:1:1 occurred, indicating the $^1O_2$ generation by US irradiated Ti_3C_2 NSs [44]. In addition, the H–Ti_3C_2-PEG NSs showed a higher ability in producing $^1O_2$ under US irradiation, revealing that the H–Ti_3C_2-PEG NSs indeed could act as better sonosensitizers than Ti_3C_2 NSs (Fig. 2e). Importantly, the inorganic sonosensitizer had the advantages of good ultrasonic stability and continuous ROS generation. To evaluate ROS generation stability, the H_H-Ti_3C_2-PEG NSs were treated with US for five cycles, and the stability performance was reflected by the decline of DPBF probe, which showed no significant change (Fig. 2f, Fig. S13). Moreover, after US irradiation for different times, the UV–vis–NIR absorbance spectra and the DLS sizes of H_H-Ti_3C_2-PEG NSs had no obvious change. Therefore, the H_H-Ti_3C_2-PEG NSs possessed excellent stability under US irradiation

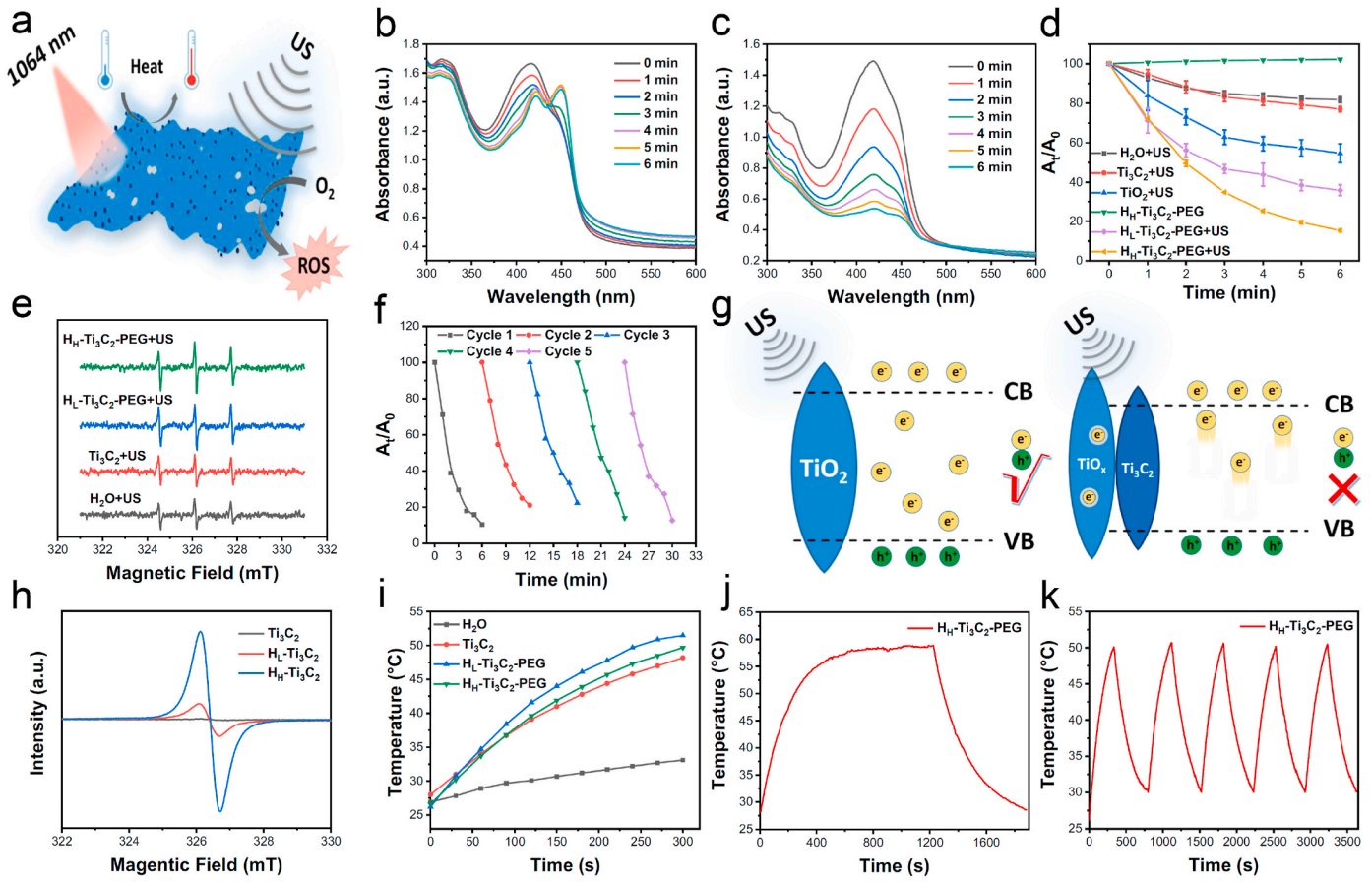

Fig. 2. Sonodynamic and photothermal performance of Ti_3C_2 NSs, H_L-Ti_3C_2-PEG NSs, and H_H-Ti_3C_2-PEG NSs. (**a**) The schematic illustration of sonodynamic and photothermal properties of H–Ti_3C_2-PEG NSs. (**b&c**) ROS generation by the Ti_3C_2 NSs (**b**) and H_H-Ti_3C_2-PEG NSs (**c**) with DPBF under US irradiation. (**d**) Comparison of the sonodynamic performance of H_2O, commercial TiO_2, Ti_3C_2 NSs, H_L-Ti_3C_2-PEG NSs, and H_H-Ti_3C_2-PEG NSs detected by DPBF probe (n = 3 independent samples). (**e**) The ESR spectra showing ROS ($^1O_2$) generation for H_2O, Ti_3C_2 NSs, H_L-Ti_3C_2-PEG NSs, and H_H-Ti_3C_2-PEG NSs under the same US irradiation. (**f**) The ROS generation stability of the H_H-Ti_3C_2-PEG NSs with DPBF under US irradiation in five cycles. (**g**) The mechanism of TiO_2 NPs and H–Ti_3C_2-PEG NSs under US irradiation. (**h**) The ESR spectra demonstrating the oxygen vacancy signal of Ti_3C_2 NSs, H_L-Ti_3C_2 NSs, and H_H-Ti_3C_2 NSs at g = 2.03. (**i**) The photothermal heating curves of H_2O, Ti_3C_2 NSs, H_L-Ti_3C_2-PEG NSs, and H_H-Ti_3C_2-PEG NSs (50 ppm, 1W·cm^{-2}). (**j**) The photothermal profile of H_H-Ti_3C_2-PEG NSs after 1064 nm laser exposure to obtain steady temperature and turn off the laser to cool down. (**k**) The heat stability of H_H-Ti_3C_2-PEG NSs in five cycles laser On/Off. Error bars = standard deviation (n = 3). Data are presented as mean values ± SD. A representative image of three biological replicates from each group is shown.

(Fig. S14).

Next, the mechanism of enhanced SDT efficiency by the H–Ti_3C_2 NSs was systematically investigated. As an important semiconductor photocatalyst, the formed TiO_x on the surface of Ti_3C_2 NSs with different oxidation degrees could promote the separation of e^--h^+, which could improve the ROS generation efficiency. Meanwhile, Ti_3C_2 NSs treated by the high-temperature might generate a large amount of oxygen vacancy (V_o) that could capture the e^- to prevent the recombination of e^--h^+ pairs, thus ulteriorly increasing the ROS generation effect. Therefore, to prove the above sonodynamic mechanism of H–Ti_3C_2-PEG NSs, the room-temperature ESR was measured, which could determine the V_o of the sample [45,46]. The Ti_3C_2 NSs, H_L-Ti_3C_2-PEG NSs, and H_H-Ti_3C_2--PEG NSs revealed the V_o signal located at g = 2.03, and the signal intensity was gradually enhanced with the prolonged high-temperature treatment time (Fig. 2h), indicating that the V_o structure could improve the ability to capture e^-. Furthermore, the photoluminescence (PL) spectra of Ti_3C_2 NSs, H_L-Ti_3C_2-PEG NSs, and H_H-Ti_3C_2-PEG NSs were future measured to determine the oxygen vacancy structure. The PL spectra showed that the emission intensities of H_L-Ti_3C_2-PEG NSs and H_H-Ti_3C_2-PEG NSs were much lower than that of Ti_3C_2 NSs (Fig. S15), probably due to that most of the V_o in H_H-Ti_3C_2-PEG NSs could capture the photo-excited electrons, then the decreased excite energy reduced the emission intensity. According to the above results, the probable mechanism was confirmed as fellows (Fig. 2g). Owing to the TiO_x formation on the surface of Ti_3C_2 NSs, the electron transfer could be accelerated from the valence band (VB) to the conduction band (CB) when receiving the US irradiation. More importantly, the V_o of Ti_3C_2 NSs treated by high-temperature could capture e^- and prevent the recombination of e^--h^+ pairs. Therefore, the O_2 molecules captured the e^- and generated large amounts of $^1O_2$, leading to the high generation efficiency of ROS (for example, $^1O_2$) with H–Ti_3C_2 NSs rather than Ti_3C_2 NSs under US irradiation. In brief, the formation of TiO_x and oxygen vacancy of Ti_3C_2 NSs contributed to the improved sonodynamic effect.

The optical properties of the Ti_3C_2-PEG NSs were studied afterwards. Similar to the Ti_3C_2 NSs, both H_L-Ti_3C_2-PEG NSs and H_H-Ti_3C_2-PEG NSs had good absorbance in NIR I and NIR II regions (Fig. S16). Because the laser of NIR II (1000–1700 nm) has a higher tissue penetration depth than NIR I (700–1000 nm), the 1064 nm laser was selected here as the excitation source for potential PTT. The photothermal performance of Ti_3C_2 NSs, H_L-Ti_3C_2-PEG NSs, and H_H-Ti_3C_2-PEG NSs showed similar results at the concentration of 50 ppm (Ti ions) under the NIR II laser irradiation (Fig. 2i). For the comprehensive assessment, the photothermal property of Ti_3C_2 NSs, H_L-Ti_3C_2-PEG NSs, and H_H-Ti_3C_2-PEG NSs at the various concentration (0, 25, 50, 100, and 200 ppm) and various power densities (0.5, 0.75, 1, 1.25, and 1.5 W ■ cm^{-2}) were carefully investigated (Fig. S17), and the photothermal curves showed

the concentration-dependent and power-dependent behavior of Ti_3C_2 NSs before and after high-temperature treatment. Furthermore, the photothermal conversion efficiency (η) of Ti_3C_2 NSs and H_H-Ti_3C_2 NSs was calculated to be ~50.8% and ~49.6%, respectively, much higher than the previously reported Ti_3C_2-based PTT agents (Fig. 2j, Fig. S18). To evaluate the photothermal stabilities of H_H-Ti_3C_2-PEG NSs, the laser on/off through five cycles and the photothermal absorbance were not changed obviously, which showed excellent photothermal stability (Fig. 2k, Fig. S19).

2.3. *In vitro Sonodynamic and photothermal performance of H–Ti_3C_2-PEG NSs*

Based on the above results, the H_H-Ti_3C_2-PEG NSs possessed great photothermal and sonodynamic efficiency. Next, the *in vitro* PTT and SDT properties of H_H-Ti_3C_2 NSs were evaluated (Fig. 3a). Firstly, the cytotoxicity of the H_H-Ti_3C_2-PEG NSs was assessed by the standard methyl thiazolyl tetrazolium (MTT) assay, which showed that H_H-Ti_3C_2-PEG NSs had no obvious cytotoxicity even the concentration was as high as 100 μg mL^{-1} at the different incubation time (6, 12, and 24 h) (Fig. 3b). Next, the standard MTT assay was utilized to evaluate the therapeutic efficiency by the H_H-Ti_3C_2-PEG NSs (Fig. 3c). Using 1064 nm laser irradiation for 10 min (<1 W ■ cm^{-1}), the temperature of the cell culture medium maintained at ~ 42 °C, and the cell viability was as high as ~79.5%. When the cells were irradiated by US only (40 KHz, 3W ■ cm^{-1}, 1 min per cycle, 5 cycles), the cell viability was decreased to ~ 53.4%. Interestingly, the cell viability was as low as ~13.4% with the combined 1064 nm laser irradiation and then US treatment. It might be the reason that the mild photothermal effect promoted the endocytosis and enhanced efficiency of SDT. To verify this hypothesis, the Cy5.5-labeled H_H-Ti_3C_2-PEG NSs were incubated with 4T1 cells for different times. It could be found that the fluorescence intensity of Cy5.5 increased with time, and the group of H_H-Ti_3C_2-PEG NSs plus laser irradiation showed a higher fluorescence intensity than that in the H_H-Ti_3C_2-PEG NSs group (Fig. 3d and e). confirmed the hypothesis that the mild photothermal effect could improve the efficiency of SDT by promoting the endocytosis of H_H- Ti_3C_2-PEG NSs.

Next, the live/dead co-staining assay was conducted and further confirmed that the mild PTT could enhance the SDT therapeutic effect (Fig. 3g). It also found that the mild photothermal effect could improve the cell membrane permeability and increase the cellular uptake of the H_H-Ti_3C_2-PEG NSs. To further demonstrate the treatment, the study of apoptosis assay based on the typical Annexin V-FITC and PI was conducted (Fig. 3f). The cell viabilities in the groups of H_H-Ti_3C_2-PEG + Laser and H_H-Ti_3C_2-PEG + US were ~85.8% and ~74.9%, respectively, however, the majority of cells were killed by the H_H-Ti_3C_2-PEG + Laser + US, with only ~4% of cells survived. To investigate the mechanism of cell apoptosis by the H_H-Ti_3C_2-PEG NSs, the ROS staining assay was tested by using 2,7 - dichlorofluorescein diacetate (DCFH-DA, green color). The strongest green signal was observed in the group of H_H-Ti_3C_2-PEG NSs + Laser + US, indicating that the enhanced uptake of H_H-Ti_3C_2-PEG NSs by the mild photothermal effect was helpful for a large amount of ROS generation under US irradiation, as compared with that of H_H-Ti_3C_2-PEG NSs + US group (Fig. 3h, Fig. S20). These results demonstrated that the mild photothermal could promote endocytosis and the H_H-Ti_3C_2-PEG NSs could generate ROS under US irradiation to kill the cancer cells.

For evaluating the synergistic effect of H_H-Ti_3C_2-PEG NSs *in vivo*, the blood circulation was firstly studied to monitor the biocompatibility and tumor accumulation potential. After the intravenous (i.v.) injection of H_H-Ti_3C_2-PEG NSs into the Balb/c mice bearing 4T1 tumor, the pharmacokinetics indicated that the H_H-Ti_3C_2-PEG NSs had good biocompatibility and stability (Fig. 4a). It would be more accurate to know the concentration of H_H-Ti_3C_2-PEG NSs in the tumor site, which could help to design the optimal schedule to initiating treatment and reducing the damage to the surrounding normal tissue. Then photoacoustic (PA) imaging was used to investigate the biodistribution owing to the great absorbance in NIR windows. *In vitro* PA imaging showed that the higher concentration of the H_H-Ti_3C_2-PEG NSs, the stronger the PA signal (Fig. 4b, Fig. S21). *In vivo* PA imaging demonstrated that PA signal located at the tumor site became stronger with the prolonged circulating time due to the enhanced permeability and retention (EPR) effect, with the highest signal appeared in the tumor site at 12 h post injection, and it could retain in the tumor site for a longer time, providing the long-term window for cancer treatment (Fig. 4c and d). Afterwards, the biodistribution of H_H-Ti_3C_2-PEG NSs in the tumor was quantitatively analyzed by inductively coupled plasma optical emission spectrometry (ICP-OES) to determine Ti ions. It could be found that the tumor uptake of the H_H-Ti_3C_2-PEG NSs was ~5.8% ID g^{-1} after i. v. Injection for 12 h, evidencing an efficient tumor accumulation of the H_H-Ti_3C_2-PEG NSs (Fig. 4e).

2.4. *In vivo Sonodynamic and photothermal performance of H–Ti_3C_2-PEG NSs*

Encouraged by the excellent properties indicated by the *in vitro* studies, the *in vivo* sonodynamic and photothermal performances of H–Ti_3C_2-PEG NSs were investigated. First of all, the *in vivo* photothermal property of the H_H-Ti_3C_2-PEG NSs for the NIR II laser-induced hyperthermia was studied (Fig. 4f). 4T1 tumor-bearing mice were exposed to the 1064 nm laser irradiation after i. v. Injection for 12 h (1 W ■ cm^{-2}, 5 min), then the tumor temperature was quickly increased to ~50.3 °C, that can achieve the condition of mild photothermal. (Fig. S22). However, the temperature of the control group was less increased, mainly due to the strong NIR II absorbance and the efficient tumor accumulation of the H_H-Ti_3C_2-PEG NSs. The complex TME and abnormal blood vessels lead to severe hypoxia in the solid tumor, which greatly reduces the therapeutic effect of ROS. Based on the previous reports, the mild photothermal effect could promote blood circulation and increase the number of red blood cells, thus increasing the oxygen-carrying capacity of hemoglobin, which could reverse the hypoxic microenvironment and increase the effect of ROS-based therapies [22,47]. PA imaging of oxyhemoglobin saturation was detected in disparate points after irradiation with different times (5 min, 15 min, 25 min, T < 42 °C). It was obvious that the blood oxygen was time-dependent enhanced and reached the maximum at 10 min (Fig. S23). Later, an immune-fluorescence hypoxia staining assay was conducted (Fig. 4g). The hypoxia signals of the H_H-Ti_3C_2-PEG NSs + Laser group were significantly decreased compared with other control groups, which suggested that the mild photothermal effect could relieve the tumor hypoxia, so that the sonodynamic effect could be enhanced.

Then, we studied the anti-tumor effect of the H_H-Ti_3C_2-PEG NSs via the mild PTT- enhanced SDT of the 4T1 tumor-bearing mice (Fig. 5a). All the mice were randomly divided into seven group: (1) control; (2) H_H-Ti_3C_2-PEG NSs (i.v. Injection, 20 mg ■ kg^{-1}); (3) Laser (1064 nm, < 1W ■ cm^{-2}, 15min, T < 42 °C); (4) US (40 kHz, 3W ■ cm^{-2}, 1 min per cycle, 15 cycles); (5) H_H-Ti_3C_2-PEG NSs + Laser; (6) H_H-Ti_3C_2-PEG NSs + US; (7) H_H-Ti_3C_2-PEG NSs + Laser + US. The H_H-Ti_3C_2-PEG NSs were administrated intravenously. According to the above PA imaging results, the 1064 nm laser and US irradiation were subsequently applied to the tumors after 12 h post injection. After treatments, the tumor growth of different groups was monitored (Fig. 5b). Compared with the control group, the tumors grew rapidly in the groups of H_H-Ti_3C_2-PEG NSs, Laser, US, and H_H-Ti_3C_2-PEG NSs + Laser, but slowly in the H_H-Ti_3C_2-PEG NSs + US group, which showed a certain inhibitory effect, indicating that the H_H-Ti_3C_2-PEG NSs had a good sonodynamic effect for tumor inhibition. From the tumor inhibitory rate statistics, the groups of H_H-Ti_3C_2-PEG NSs, Laser, US, and H_H-Ti_3C_2-PEG NSs + Laser only had the extremely low inhibitory effect, while the H_H-Ti_3C_2-PEG NSs + US group possessed ~54.9% inhibitory rate, and yet the tumors could not achieve ablation thoroughly. When treated with H_H-Ti_3C_2-PEG NSs + Laser + US, the tumors were completely suppressed (Fig. 5c), probably

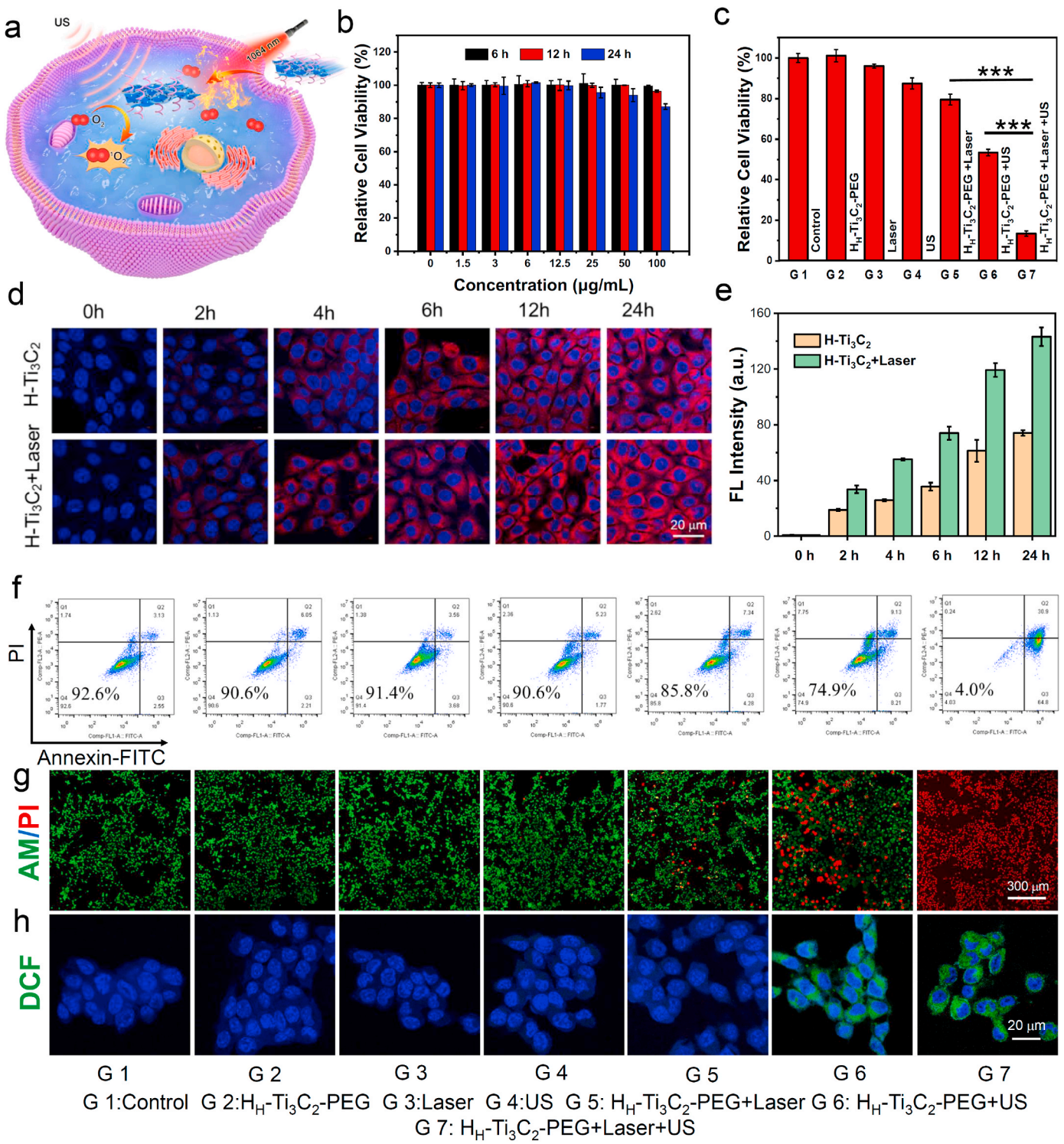

Fig. 3. ***In vitro*** **mild PTT-enhanced SDT of H_H-Ti_3C_2-PEG NSs.** (**a**) Schematic illustrating of H_H-Ti_3C_2-PEG NSs for the mild PTT-enhanced SDT. (**b**) Relative cell viability of 4T1 cells with the H_H-Ti_3C_2-PEG NSs with various concentrations for 6, 12, and 24 h (n = 6 biologically independent samples). (**c**) Relative cell viability of 4T1 cells after different treatments (G 1-G 7, detailed at the end of the caption) (***P < 0.001, **P < 0.01, or *P < 0.05). (**d**) Confocal images of 4T1 cells incubated with Cy5.5-conjugated H_H-Ti_3C_2-PEG NSs for different times with/without 1064 nm laser irradiation. (**e**) Quantitative analysis of the fluorescence intensity in (**d**) (n = 6 cells examined over independent micrographs). (**f**) Flow-cytometry apoptosis assay of 4T1 cells after different treatments stained with Annexin-FITC and PI. (**g**) Confocal images of 4T1 cells after incubation H_H-Ti_3C_2-PEG NSs followed by staining with Calcein AM (green, live cells) and propidium iodide (red, dead cells) after different treatments (G 1-G 7). (**h**) Confocal images of 4T1 cells stained with DAPI (blue, nuclei) and DCFH-DA (green, intracell ROS) after various treatments (G 1-G 7). G 1: Control, G 2: H_H-Ti_3C_2-PEG, G 3: Laser, G 4: US, G 5: H_H-Ti_3C_2-PEG + Laser, G 6: H_H-Ti_3C_2-PEG + US, G 7: H_H-Ti_3C_2-PEG + Laser + US. H_H-Ti_3C_2–PEG NSs: 50 ppm, NIR laser: 1064 nm, < 1W ∎ cm^{-2}, 10 min, T < 42 °C; US irradiation: 40 kHz, 3W ∎ cm^{-2}, 1 min per cycle, 5 cycles. Error bars = standard deviation (n = 6). Data are presented as mean values ± SD. A representative image of three biological replicates from each group is shown.

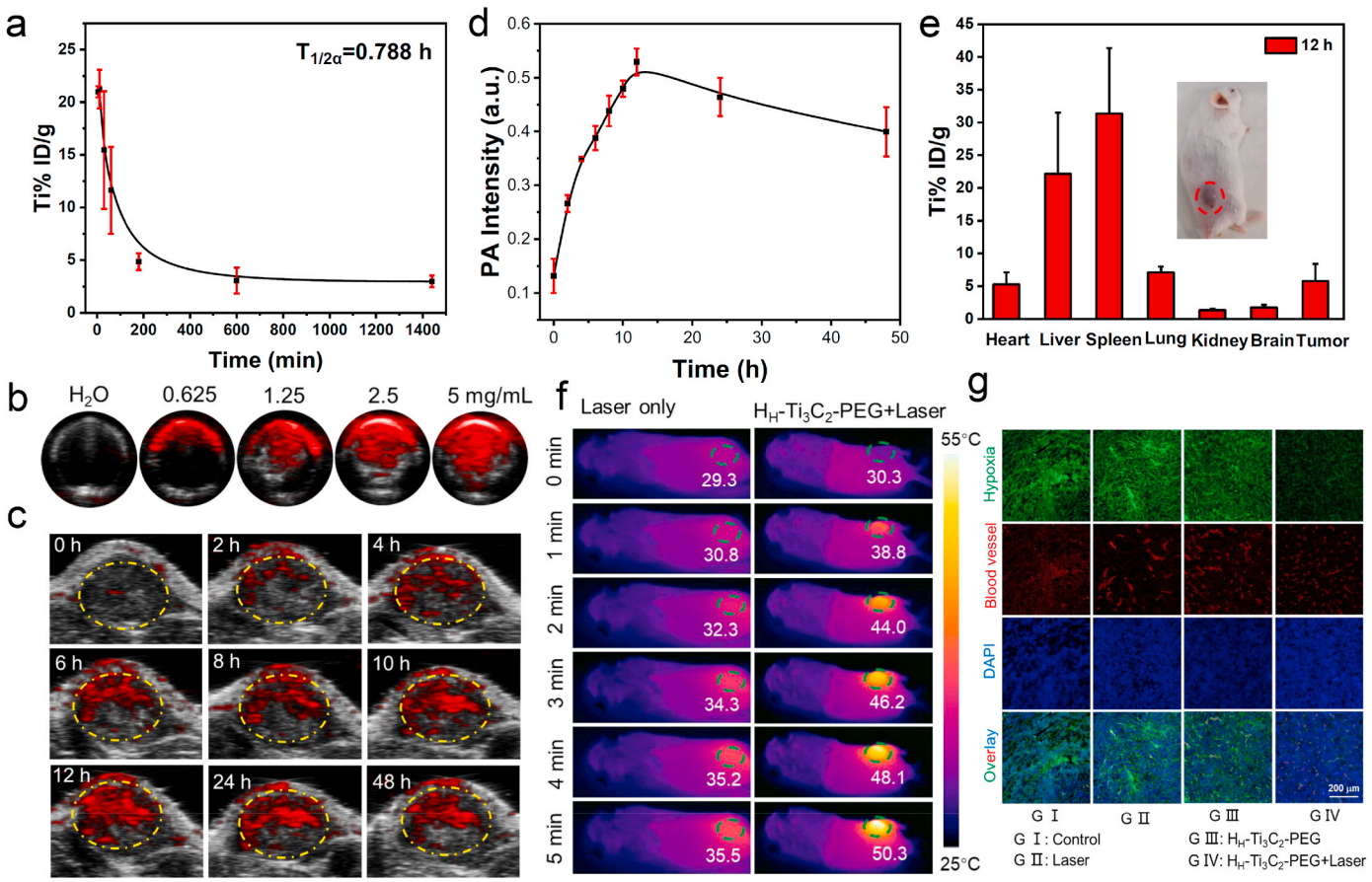

Fig. 4. ***In vivo*** **tumor accumulation and mild PTT-defeated tumor hypoxia via H_H-Ti_3C_2-PEG NSs.** (**a**) Blood circulation of H_H-Ti_3C_2-PEG NSs post i. v. injection. (**b**) PA imaging of H_H-Ti_3C_2-PEG NSs. (**c**) *In vivo* PA imaging of 4T1 tumor-bearing mice. (**d**) Time-dependent tumor PA signals at 800 nm based on PA imaging data in (**c**). (**e**) Biodistribution of H_H-Ti_3C_2-PEG NSs in mice after 12 h by i. v. injection. (**f**) IR thermal images of 4T1 tumors under the 1064 nm laser irradiation. (**g**) Tumor slices staining of different treatments. H_H-Ti_3C_2–PEG NSs: 20 mg ■ kg^{-1}; NIR laser: 1064 nm, < 1W ■ cm^{-2}, 15 min (n = 3 biologically independent mice). Data are presented as mean values ± SD.

due to that the mild photothermal effect alleviated the hypoxic microenvironment, which further enhanced SDT efficiency. Importantly, the tumors in H_H-Ti_3C_2-PEG NSs + Laser + US group did not recur, which significantly increased the overall survival. However, the size of tumors in the other control groups reached the death criteria gradually, revealing that the mild photothermal-enhanced SDT had an obvious synergistically therapeutic outcome with the H_H-Ti_3C_2-PEG NSs (Fig. 5d).

To further explore the mechanism of synergistic therapy mediated by H_H-Ti_3C_2-PEG NSs, the ROS levels in the tumors after the various treatments were evaluated via DCFH-DA staining (Fig. 5e). It was clear that the groups of control, H_H-Ti_3C_2-PEG NSs, Laser, US, and H_H-Ti_3C_2-PEG NSs + Laser only induced weak green fluorescence in tumor slices, while the groups of H_H-Ti_3C_2-PEG NSs + US and H_H-Ti_3C_2-PEG NSs + Laser + US showed enhanced green fluorescence in the tumor slices. The strongest green fluorescence intensity appeared in H_H-Ti_3C_2-PEG NSs + Laser + US group, and the intensity was 2.8 -fold higher than that of the control group (Fig. S24). Therefore, the mild PTT could alleviate the hypoxic tumor environment and promote the generation of ROS under US irradiation. Thereafter, the hematoxylin and eosin (H&E) staining of tumor slides was conducted after the various treatments at 24 h (Fig. 5f). In the groups of H_H-Ti_3C_2-PEG NSs + US and H_H-Ti_3C_2-PEG NSs + Laser + US, nearly all the tumor cells were damaged severely while the other groups had little impact on tumor cells. These results confirmed that the mild PTT could enhance the efficacy of SDT to achieve a good synergistic effect by the H_H-Ti_3C_2-PEG NSs.

Lastly, biosafety is the most important issue to be considered for the wide biomedicine application of nanomaterials, especially for inorganic nanomaterials [48,49]. Firstly, the H&E staining showed that the main organs (heart, liver, spleen, lung, kidney, and brain) of mice had no obvious morphological changes in different time (Fig. 6a). Then, we moved to study the degradation behavior of the synthesized H_H-Ti_3C_2-PEG NSs. The H_H-Ti_3C_2-PEG NSs were dispersed in various solutions of H_2O, PBS, and RPMI (10% FBS) at 37 °C for different incubation times (Fig. 6b–d). According to the UV–vis–NIR spectra, the absorbance of H_H-Ti_3C_2-PEG NSs around 808 nm decreased after 21 days, and the photograph of H_H-Ti_3C_2-PEG NSs showed the fading color, which evidenced the biodegradation of H_H-Ti_3C_2-PEG NSs. However, a relatively smaller change in the 1640 cell culture medium, probably due to the reason that the cell culture medium contained 10% FBS could partially protect the degradation of Ti_3C_2 nanosheets. Furthermore, TEM and XRD were used to explore the morphology and component after the biodegradation of H_H-Ti_3C_2-PEG NSs. TEM image showed the mixture of nanosheets and nanodots, and the XRD patterns should the amorphous structure in the process the degradation (Fig. S25). Next, we discovered the *in vivo* distribution profile and the metabolic pathway of H_H-Ti_3C_2-PEG NSs (Fig. 6e and f). At 24 h after i. v. injection, the biodistribution showed the relatively high accumulation of H_H-Ti_3C_2-PEG NSs in liver (~36.5% ± 1.8% ID g^{-1}), spleen (~38% ± 3.0% ID g^{-1}), and lung (~14% ± 4.5% ID g^{-1}). However, the content dropped to 12% ± 0.6% ID g^{-1} in liver, 13.7% ± 1.8% ID g^{-1} in spleen, and 2.2% ± 0.2% ID g^{-1} in lung at the 30^{th} day later, respectively, showing that most of the H_H-Ti_3C_2-PEG NSs had been metabolized out of the body. In order to investigate the metabolism pathway of the H_H-Ti_3C_2-PEG NSs, the feces

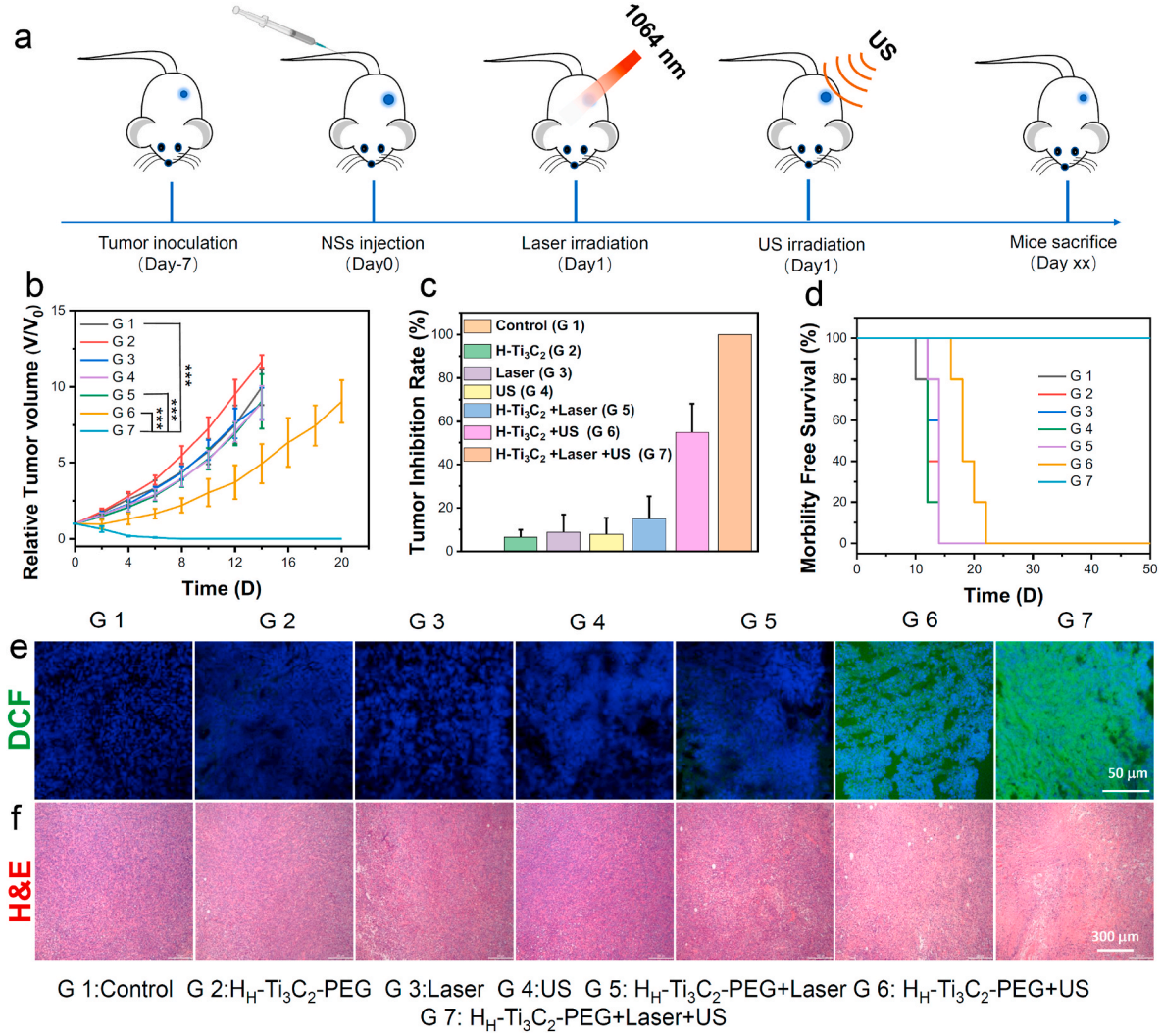

Fig. 5. ***In vivo*** **mild PTT-enhanced SDT of H_H-Ti_3C_2-PEG NSs.** (**a**) Schematic illustration to show the combination of PTT and SDT of H_H-Ti_3C_2-PEG NSs. (**b**) Average tumor growth curves on mice with different treatments (G 1-G 7, detailed at the end of the caption), (***P < 0.001, **P < 0.01, or *P < 0.05). (**c**) Tumor inhibition rates of different treatments (G 1-G 7). (**d**) Survival curves of mice after various treatments. (**e**) Micrograph of DCFH-DA stained tumor slices with different treatments. (**f**) H&E stained tumor slices G 1: Control, G 2: H_H-Ti_3C_2-PEG, G 3: Laser, G 4: US, G 5: H_H-Ti_3C_2-PEG + Laser, G 6: H_H-Ti_3C_2-PEG + US, G 7: H_H-Ti_3C_2-PEG + Laser + US. H_H-Ti_3C_2–PEG NSs: 20 mg ■ kg^{-1}; NIR laser: 1064 nm, < 1 W ■ cm^{-2}, 15 min, T < 42 °C; US irradiation: 40 kHz, 3W ■ cm^{-2}, 1 min per cycle, 15 cycles. (n = 5 biologically independent mice). Data are presented as mean values ± SD.

and urine of mice were collected to detect the content of Ti through ICP-OES. It could be found that H_H-Ti_3C_2-PEG NSs were mainly excreted through the hepatic metabolism due to the high concentration of Ti ions in the feces. Moreover, there was no significant change in the body weight of mice during the treatment, indicating that the H_H-Ti_3C_2-PEG NSs had no obvious toxicity at the injection dose (20 mg ■ kg^{-1}) (Fig. 6g). Subsequently, the blood was collected after injection of H_H-Ti_3C_2-PEG NSs for blood routine and blood biochemical tests. All these hematological indexes had no significant difference among all the groups (Fig. S26). In brief, the H_H-Ti_3C_2-PEG NSs could be used as safe sonosensitizers for enhanced SDT without causing any long-term toxicity.

3. Conclusion

In summary, the oxygen-defective Ti_3C_2 NSs (H–Ti_3C_2 NSs) were successfully established by two-step methods of chemical exfoliation and high-temperature treatment. After high-temperature treatment, the H–Ti_3C_2 NSs displayed an excellent sonodynamic efficacy, and the efficiency was enhanced by the long-time high-temperature treatment. Importantly, the oxygen defect structure of H–Ti_3C_2 NSs treated by the high-temperature also could prevent the recombination of e^--h^+ pairs, which further enhanced the sonodynamic effect under US irradiation. Meanwhile, the H–Ti_3C_2 NSs also had relatively high absorbance in the NIR II window, which could produce heat under laser irradiation. After PEGylation, the H–Ti_3C_2-PEG NSs showed great stability and biocompatibility. The good photothermal efficacy of H–Ti_3C_2-PEG NSs promoted the endocytosis of the H–Ti_3C_2-PEG NSs, and further enhanced the efficacy of SDT. *In vivo* studies showed that the mild photothermal effect could accelerate blood circulation and alleviate the hypoxia tumor microenvironment to realize PTT enhanced SDT. Importantly, the biodegradable H–Ti_3C_2 NSs were excreted out of the body without inducing any long-term toxicity. In brief, our work developed the H–Ti_3C_2 NSs as a high-efficiency and safe sonosensitizer for photothermal-enhanced SDT, which highlighted the extension of the biomedical application of MXene-based nanoplatforms.

CRediT authorship contribution statement

Guangqiang Li: Writing – review & editing, Writing – original draft,

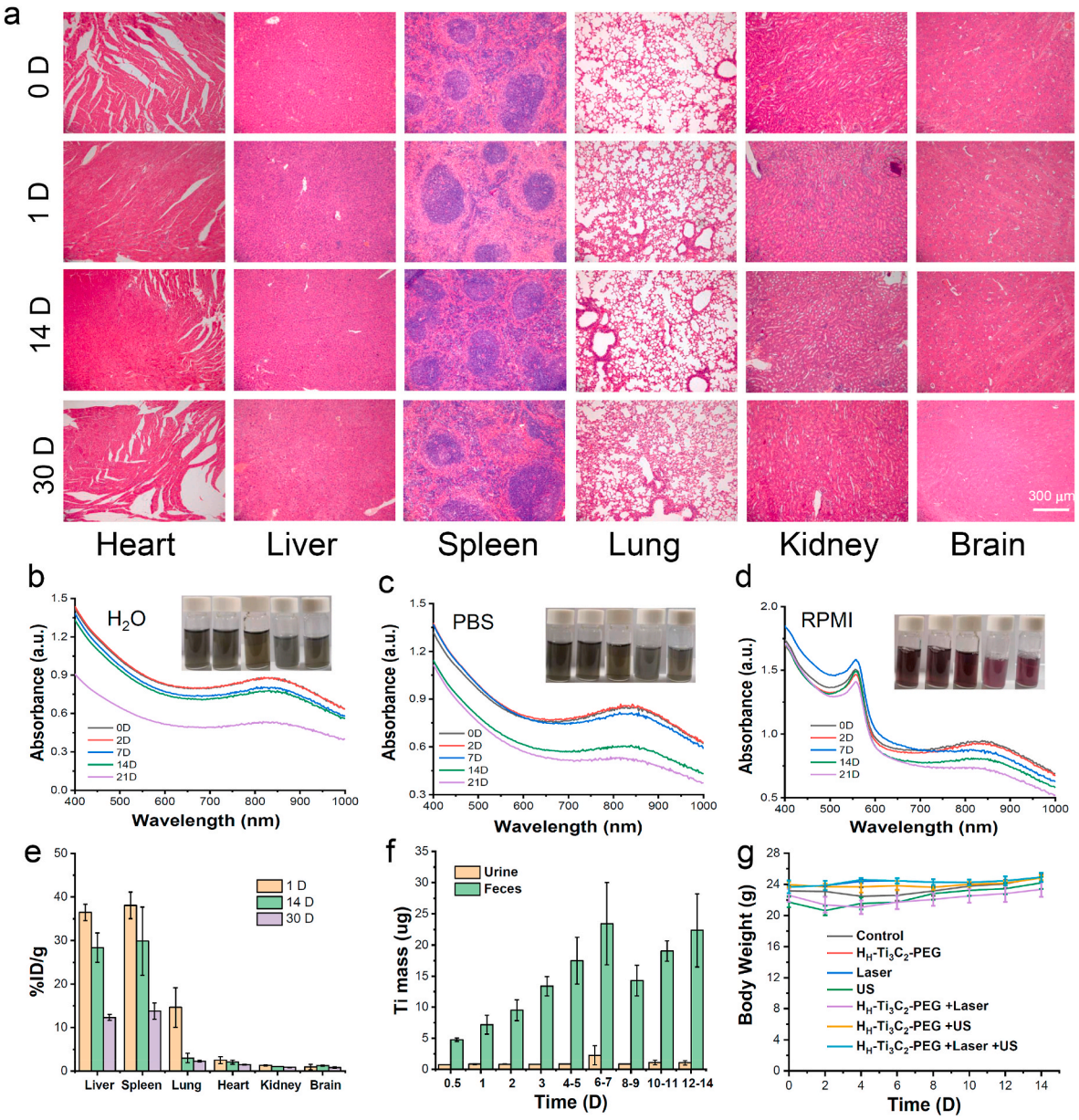

Fig. 6. Biosafety evaluation of H_H-Ti_3C_2-PEG NSs. (**a**) H&E staining of mice major organs before and post i. v. injection with H_H-Ti_3C_2-PEG NSs at 1, 14, and 30 days. (**b-d**) UV–vis–NIR spectra of H_H-Ti_3C_2-PEG NSs in H_2O (**b**), PBS (**c**), and RPMI (**d**) for different days. Insert are the corresponding photograph. (**e**) Biodistribution of H_H-Ti_3C_2-PEG NSs. (**f**) The detected Ti mass in urine and feces. (**g**) The body weight variation of mice after various treatments. (n = 5 biologically independent mice). Data are presented as mean values ± SD.

designed the experiments, synthesized the materials, performed the sonodynamic and photothermal experiments, performed the cells experiments, wrote the paper, reviewed and edited the paper. **Xiaoyan Zhong:** Writing – review & editing, Writing – original draft, performed animal experiments, wrote the paper, reviewed and edited the paper. **Xianwen Wang:** Writing – review & editing, synthesized the materials, performed the sonodynamic and photothermal experiments, reviewed and edited the paper. **Fei Gong:** Writing – review & editing. **Huali Lei:** Writing – review & editing. **Yangkai Zhou:** Writing – review & editing. **Chengfei Li:** Writing – review & editing. **Zhidong Xiao:** Writing – review & editing, Writing – original draft. **Guoxi Ren:** Writing – review & editing, Formal analysis. **Liang Zhang:** Writing – review & editing, Formal analysis. **Zhiqiang Dong:** Writing – review & editing, Formal analysis. **Zhuang Liu:** Writing – review & editing, Formal analysis. **Liang Cheng:** Writing – review & editing, Writing – original draft.

Declaration of Competing interest

The authors declare no competing financial interest.

Acknowledgment

This article was partially supported by the National Research Programs of China (2016YFA0201200), the National Natural Science Foundation of China (U20A20254, 52072253), Collaborative Innovation Center of Suzhou Nano Science and Technology, a Jiangsu Social Development Project (BE2019658), a Project Funded by the Priority Academic Program Development (PAPD) of Jiangsu Higher Education Institutions. L. Cheng was supported by the Tang Scholarship of Soochow University, and the fundamental Research Funds for Central Universities (2662019PY024). The authors thank SSRF (beamline 02B02) for the allocation of synchrotron beamtime.

Appendix A. Supplementary data

Supplementary data to this article can be found online at https://doi.org/10.1016/j.bioactmat.2021.06.021.

References

[1] S. Son, J.H. Kim, X. Wang, C. Zhang, S.A. Yoon, J. Shin, A. Sharma, M.H. Lee, L. Cheng, J. Wu, Multifunctional sonosensitizers in sonodynamic cancer therapy, Chem. Soc. Rev. 49 (2020) 3244–3261.

[2] I. Rosenthal, J.Z. Sostaric, P. Riesz, Sonodynamic therapy—a review of the synergistic effects of drugs and ultrasound, Ultrason. Sonochem. 11 (2004) 349–363.

[3] Y. Yin, X. Jiang, L. Sun, H. Li, C. Su, Y. Zhang, G. Xu, X. Li, C. Zhao, Y. Chen, H. Xu, K. Zhang, Continuous inertial cavitation evokes massive ROS for reinforcing sonodynamic therapy and immunogenic cell death against breast carcinoma, Nano Today 36 (2021) 101009.

[4] M. Liu, A.R. Khan, J. Ji, G. Lin, X. Zhao, G. Zhai, Crosslinked self-assembled nanoparticles for chemo-sonodynamic combination therapy favoring antitumor, antimetastasis management and immune responses, J. Contr. Release 290 (2018) 150–164.

[5] C. Chen, Z. Wu, P. Ding, N. Sun, H. Liu, Y. Chen, Z. Wang, R. Pei, Peptide NGR modified TiO_2 nanofiber substrate for circulating tumor cells capture, Advanced Fiber Materials 2 (2020) 186–193.

[6] J. Zhao, W. Cui, Functional electrospun fibers for local therapy of cancer, Advanced Fiber Materials 2 (2020) 229–245.

[7] K. Zhang, Y. Fang, Y. He, H. Yin, X. Guan, Y. Pu, B. Zhou, W. Yue, W. Ren, D. Du, H. Li, C. Liu, L. Sun, Y. Chen, H. Xu, Extravascular gelation shrinkage-derived internal stress enables tumor starvation therapy with suppressed metastasis and recurrence, Nat. Commun. 10 (2019) 5380.

[8] R. Bagherifar, S.H. Kiaie, Z. Hatami, A. Ahmadi, A. Sadeghnejad, B. Baradaran, R. Jafari, Y. Javadzadeh, Nanoparticle-mediated synergistic chemoimmunotherapy for tailoring cancer therapy: recent advances and perspectives, J. Nanobiotechnol. 19 (2021) 110.

[9] X. Xie, W. Gao, J. Hao, J. Wu, X. Cai, Y. Zheng, Self-synergistic effect of Prussian blue nanoparticles for cancer therapy: driving photothermal therapy and reducing hyperthermia-induced side effects, J. Nanobiotechnol. 19 (2021) 126.

[10] M. Liu, H. Du, A.R. Khan, J. Ji, A. Yu, G. Zhai, Redox/enzyme sensitive chondroitin sulfate-based self-assembled nanoparticles loading docetaxel for the inhibition of metastasis and growth of melanoma, Carbohydr. Polym. 184 (2018) 82–93.

[11] X. Wang, X. Zhong, F. Gong, Y. Chao, L. Cheng, Newly developed strategies for improving sonodynamic therapy, Materials Horizons 7 (2020) 2028–2046.

[12] X. Pan, H. Wang, S. Wang, X. Sun, L. Wang, W. Wang, H. Shen, H. Liu, Sonodynamic therapy (SDT): a novel strategy for cancer nanotheranostics, Sci. China Life Sci. 61 (2018) 415–426.

[13] L. Zhang, S. Shen, L. Cheng, H. You, L. Lu, C. Ma, Y. Dai, J. Fang, Mesoporous gold nanoparticles for photothermal controlled anticancer drug delivery, Nanomedicine 14 (2019) 1443–1454.

[14] X. Lin, J. Song, X. Chen, H. Yang, Ultrasound-activated sensitizers and applications, Angew. Chem. Int. Ed. 59 (2020) 14212–14233.

[15] X. Pan, L. Bai, H. Wang, Q. Wu, H. Wang, S. Liu, B. Xu, X. Shi, H. Liu, Metal–organic-framework-derived carbon nanostructure augmented sonodynamic cancer therapy, Adv. Mater. 30 (2018) 1800180.

[16] N. Miyoshi, T. Igarashi, P. Riesz, Evidence against singlet oxygen formation by sonolysis of aqueous oxygen-saturated solutions of hematoporphyrin and rose bengal: the mechanism of sonodynamic therapy, Ultrason. Sonochem. 7 (2000) 121–124.

[17] X. Wang, X. Zhong, Z. Liu, L. Cheng, Recent progress of chemodynamic therapy-induced combination cancer therapy, Nano Today 35 (2020) 100946.

[18] X. Han, J. Huang, X. Jing, D. Yang, H. Lin, Z. Wang, P. Li, Y. Chen, Oxygen-deficient black titania for synergistic/enhanced sonodynamic and photoinduced cancer therapy at near infrared-II biowindow, ACS Nano 12 (2018) 4545–4555.

[19] J. Xiao, Y. Zhang, T. Fang, T. Yuan, Q. Tian, J. Liu, Y. Cheng, Y. Zhu, L. Cheng, W. Cui, Mineralized manganese dioxide channel as the stent coating for in situ precise tumor navigation, Nano Research 46 (2020) 981.

[20] F. Gong, L. Cheng, N. Yang, O. Betzer, L. Feng, Q. Zhou, Y. Li, R. Chen, R. Popovtzer, Z. Liu, Ultrasmall oxygen-deficient bimetallic oxide $MnWO_X$ nanoparticles for depletion of endogenous GSH and enhanced sonodynamic cancer therapy, Adv. Mater. 31 (2019) 1900730.

[21] H. Lei, X. Wang, S. Bai, F. Gong, N. Yang, Y. Gong, L. Hou, M. Cao, Z. Liu, L. Cheng, Biodegradable Fe-doped vanadium disulfide theranostic nanosheets for enhanced sonodynamic/chemodynamic therapy, ACS Appl. Mater. Interfaces 12 (2020) 52370–52382.

[22] F. Gong, N. Yang, Y. Wang, M. Zhuo, Q. Zhao, S. Wang, Y. Li, Z. Liu, Q. Chen, L. Cheng, Oxygen-Deficient bimetallic oxide $FeWO_X$ nanosheets as peroxidase-like nanozyme for sensing cancer via photoacoustic imaging, Small 16 (2020) 2003496.

[23] K.C. Valkenburg, A.E. de Groot, K.J. Pienta, Targeting the tumour stroma to improve cancer therapy, Nat. Rev. Clin. Oncol. 15 (2018) 366–381.

[24] X. Guan, H.-H. Yin, X.-H. Xu, G. Xu, Y. Zhang, B.-G. Zhou, W.-W. Yue, C. Liu, L.-P. Sun, H.-X. Xu, K. Zhang, Tumor metabolism-engineered composite nanoplatforms potentiate sonodynamic therapy via reshaping tumor microenvironment and facilitating electron-hole pairs' separation, Adv. Funct. Mater. 30 (2020) 2000326.

[25] C.J. Gomer, A. Ferrario, M. Luna, N. Rucker, S. Wong, Photodynamic therapy: combined modality approaches targeting the tumor microenvironment, Lasers in Surgery and Medicine, The Official Journal of the American Society for Laser Medicine and Surgery 38 (2006) 516–521.

[26] Z. Tang, Y. Liu, M. He, W. Bu, Chemodynamic therapy: tumour microenvironment-mediated Fenton and Fenton-like reactions, Angew. Chem. Int. Ed. 58 (2019) 946–956.

[27] H.E. Barker, J.T. Paget, A.A. Khan, K.J. Harrington, The tumour microenvironment after radiotherapy: mechanisms of resistance and recurrence, Nat. Rev. Canc. 15 (2015) 409–425.

[28] K. Lu, C. He, N. Guo, C. Chan, K. Ni, G. Lan, H. Tang, C. Pelizzari, Y.-X. Fu, M. T. Spiotto, Low-dose X-ray radiotherapy–radiodynamic therapy via nanoscale metal–organic frameworks enhances checkpoint blockade immunotherapy, Nature biomedical engineering 2 (2018) 600–610.

[29] Y. Chao, L. Xu, C. Liang, L. Feng, J. Xu, Z. Dong, L. Tian, X. Yi, K. Yang, Z. Liu, Combined local immunostimulatory radioisotope therapy and systemic immune checkpoint blockade imparts potent antitumour responses, Nature biomedical engineering 2 (2018) 611–621.

[30] X. Zhong, X. Wang, L. Cheng, Y.a. Tang, G. Zhan, F. Gong, R. Zhang, J. Hu, Z. Liu, X. Yang, GSH-depleted PtCu3 nanocages for chemodynamic-enhanced sonodynamic cancer therapy, Adv. Funct. Mater. 30 (2020) 1907954.

[31] J. Chen, H. Luo, Y. Liu, W. Zhang, H. Li, T. Luo, K. Zhang, Y. Zhao, J. Liu, Oxygen-Self-produced nanoplatform for relieving hypoxia and breaking resistance to sonodynamic treatment of pancreatic cancer, ACS Nano 11 (2017) 12849–12862.

[32] K. Zhang, H. Xu, X. Jia, Y. Chen, M. Ma, L. Sun, H. Chen, Ultrasound-triggered nitric oxide release platform based on energy transformation for targeted inhibition of pancreatic tumor, ACS Nano 10 (2016) 10816–10828.

[33] Q. Chen, L. Feng, J. Liu, W. Zhu, Z. Dong, Y. Wu, Z. Liu, Intelligent albumin–MnO_2 nanoparticles as pH-/H_2O_2-responsive dissociable nanocarriers to modulate tumor hypoxia for effective combination therapy, Adv. Mater. 28 (2016) 7129–7136.

[34] X. Song, L. Feng, C. Liang, K. Yang, Z. Liu, Ultrasound triggered tumor oxygenation with oxygen-shuttle nanoperfluorocarbon to overcome hypoxia-associated resistance in cancer therapies, Nano Lett. 16 (2016) 6145–6153.

[35] K. Huang, Z. Li, J. Lin, G. Han, P. Huang, Two-dimensional transition metal carbides and nitrides (MXenes) for biomedical applications, Chem. Soc. Rev. 47 (2018) 5109–5124.

[36] W. Tang, Z. Dong, R. Zhang, X. Yi, K. Yang, M. Jin, C. Yuan, Z. Xiao, Z. Liu, L. Cheng, Multifunctional two-dimensional core–shell mxene@ gold nanocomposites for enhanced photo–radio combined therapy in the second biological window, ACS Nano 13 (2018) 284–294.

[37] H. Lin, X. Wang, L. Yu, Y. Chen, J. Shi, Two-dimensional ultrathin MXene ceramic nanosheets for photothermal conversion, Nano Lett. 17 (2017) 384–391.

[38] J. Xuan, Z. Wang, Y. Chen, D. Liang, L. Cheng, X. Yang, Z. Liu, R. Ma, T. Sasaki, F. Geng, Organic-base-driven intercalation and delamination for the production of functionalized titanium carbide nanosheets with superior photothermal therapeutic performance, Angew. Chem. 128 (2016) 14789–14794.

[39] J. Low, L. Zhang, T. Tong, B. Shen, J. Yu, TiO_2/MXene Ti_3C_2 composite with excellent photocatalytic CO_2 reduction activity, J. Catal. 361 (2018) 255–266.

[40] R. Lotfi, M. Naguib, D.E. Yilmaz, J. Nanda, A.C. Van Duin, A comparative study on the oxidation of two-dimensional Ti_3C_2 MXene structures in different environments, J. Mater. Chem. 6 (2018) 12733–12743.

[41] Z. Miao, G. Wang, X. Zhang, X. Dong, Oxygen vacancies modified TiO_2/Ti_3C_2 derived from MXenes for enhanced photocatalytic degradation of organic pollutants: the crucial role of oxygen vacancy to Schottky junction, Appl. Surf. Sci. 528 (2020) 146929.

[42] C. Wang, S. Chen, L. Song, Tuning 2D MXenes by surface controlling and interlayer engineering: methods, properties, and synchrotron radiation characterizations, Adv. Funct. Mater. 30 (2020) 2000869.

[43] Y. Xu, S. Wang, J. Yang, B. Han, R. Nie, J. Wang, J. Wang, H. Jing, In-situ grown nanocrystal TiO_2 on 2D Ti_3C_2 nanosheets for artificial photosynthesis of chemical fuels, Nanomater. Energy 51 (2018) 442–450.

[44] S.S. Kumar, T. Devasagayam, B. Bhushan, N. Verma, Scavenging of reactive oxygen species by chlorophyllin: an ESR study, Free Radic. Res. 35 (2001) 563–574.

[45] A. Bandyopadhyay, D. Ghosh, S.K. Pati, Effects of point defects on the magnetoelectronic structures of MXenes from first principles, Phys. Chem. Chem. Phys. 20 (2018) 4012–4019.

[46] L. Zhang, Q. Chen, X. Zou, J. Chen, L. Hu, Z. Dong, J. Zhou, Y. Chen, Z. Liu, L. Cheng, Intelligent protein-coated bismuth sulfide and manganese oxide nanocomposites obtained by biomineralization for multimodal imaging-guided enhanced tumor therapy, J. Mater. Chem. B 7 (2019) 5170–5181.

[47] F. Gong, N. Yang, X. Wang, Q. Zhao, Q. Chen, Z. Liu, L. Cheng, Tumor microenvironment-responsive intelligent nanoplatforms for cancer theranostics, Nano Today 32 (2020) 100851.

[48] M. Qiu, A. Singh, D. Wang, J. Qu, M. Swihart, H. Zhang, P.N. Prasad, Biocompatible and biodegradable inorganic nanostructures for nanomedicine: silicon and black phosphorus, Nano Today 25 (2019) 135–155.

[49] C.N. Loynachan, A.P. Soleimany, J.S. Dudani, Y. Lin, A. Najer, A. Bekdemir, Q. Chen, S.N. Bhatia, M.M. Stevens, Renal clearable catalytic gold nanoclusters for in vivo disease monitoring, Nat. Nanotechnol. 14 (2019) 883–890.